

# **HiSST: 4th International Conference on High-Speed Vehicle Science Technology**

22-26 September 2025, Tours, France



# Numerical investigation of acoustic perturbations radiated from a transitional and turbulent boundary layer in hypersonic wind tunnel flow conditions

Vianney Dubois <sup>1</sup>, Mathieu Lugrin <sup>2</sup>, Julien Dandois <sup>2</sup>

# **Abstract**

Direct numerical simulations of transitional and turbulent hypersonic boundary layers are performed on a flat plate geometry to reproduce the free stream acoustic perturbations observed in conventional hypersonic wind tunnels. Transition of the boundary layer is achieved through volume forcing computed either from optimal perturbation modes obtained with a resolvent-based linear stability analysis or following a random forcing approach. This numerical setup allows to simulate the noise radiation not only from the turbulent region but also from the transition region. For all three cases, the characteristics of the noise generated by the turbulent region compare well with existing data. When using a harmonic forcing to trigger the transition, the spectral content of the transition region is reflected into the acoustic perturbations originating from this region, whereas the radiation from the turbulent region shows broadband spectra.

**Keywords**: hypersonic, wind tunnel, acoustic, perturbation, DNS

#### **Nomenclature**

Latin

 $Re_1$  unit length Reynolds number U/v

 $\mathcal{R}$  resolvent operator  $\mathcal{J}$  Jacobian operator

**q** state vector  $[\rho, \rho U, \rho V, \rho W, \rho E]^T$ 

**f** forcing vector

Greek

β transverse wavenumber

 $\mu^2$  resolvent energy gain

#### Superscripts

+ dimensionless quantity (inner scales)

' fluctuating quantity

Fourier mode

#### Subscripts

∞ free stream conditionsi stagnation quantity

#### 1. Introduction

The design process of hypersonic aerospace vehicles involves the evaluation of aerothermodynamic performances, which can require the assessment of boundary layer laminar/turbulent transition since the nature of the boundary layer constrains aerodynamic [1] and thermal [2] performances. The complex nature of transitional phenomena can lead to the use of wind tunnel testing to complement analytical and numerical approaches. However, most hypersonic wind tunnel test sections show free stream fluctuation levels much higher than free flight levels [3]. Because the mechanisms at play in transitional regions depend on the incoming airflow free stream fluctuations, wind tunnel testing can lead to non-representative data. Kovasznay [4] demonstrated that compressible flows can be subjected to vortical, entropic, and acoustic perturbations. While vorticity and entropy disturbances are convected along streamlines from the settling chamber, acoustic waves propagate along characteristic curves and can originate from other sources [5]. Experimental work in supersonic and low hypersonic wind tunnels by Laufer [6, 7] highlighted that the intensity of acoustic perturbations increases with the wind tunnel Mach number, and the pressure disturbance mode becomes dominant in hypersonic facilities. These

<sup>&</sup>lt;sup>1</sup>DAAA, ONERA, Institut Polytechnique de Paris, 92190 Meudon, France, vianney.dubois@onera.fr

<sup>&</sup>lt;sup>2</sup>DAAA, ONERA, Institut Polytechnique de Paris, 92190 Meudon, France

perturbations have been found to originate from the turbulent boundary layers on the nozzle wall. The noise radiation mechanism can be modelled using the eddy Mach wave radiation theory from Phillips [7, 8]: the relative supersonic motion of turbulent structures in the local mean flow generates wavelets that propagate in the free stream region. Effects of higher fluctuation levels in the test section include a modification of the transition onset location, and opposite conclusions regarding design trends obtained from noisy or quiet data [3]. Recent numerical studies make use of direct numerical simulations (DNS) of turbulent boundary layers in hypersonic wind tunnel flow conditions, for various geometries: flat plate [9], quasi-two-dimensional wind tunnel nozzle [10], and axisymmetric wind tunnel nozzle [11]. These studies have been able to reproduce the experimental characteristics of free stream acoustic fluctuations, and provided additional insights into the nature of the disturbance fields.

These DNSs are using a turbulent inflow condition to simulate a fully turbulent boundary layer flow. As a result, the characteristics of the noise generated by the transition region of the boundary layer have not been studied, and attention must be paid to avoid acoustic radiation from the turbulent inflow [9]. The present work aims at developing a numerical workflow for direct numerical simulations of transitional and turbulent hypersonic boundary layers to study the noise generated by the transition region and by the turbulent flow developing downstream.

The transition of a boundary layer can involve a receptivity process through which free stream disturbances will excite the modal growth of convective instabilities [12]. Simulations of "controlled" transitions can be performed by exciting a specific unstable mode, while the transition can also be achieved by injecting broadband noise [13] to let the receptivity process select the most energetic disturbance modes. The present work explores both approaches by implementing a volume forcing of optimal perturbation modes, and adding a region of randomly excited source terms. The numerical approach allows to adjust the amplitude of the forcing terms to achieve similar transition location for all cases, allowing for a comparison of the radiated acoustic perturbations.

With the objective of preparing future reproductions of a noisy hypersonic wind tunnel environment, the present work is conducted on a zero-pressure gradient isothermal flat plate. This canonical geometry enables to set up numerical tools and methods, and provides data regarding noise radiation from transitional and turbulent boundary layer flows.

## 2. Numerical setup and method

#### 2.1. Geometry and flow conditions

This work studies the boundary layer that develops on a flat plate geometry placed under flow conditions that are typical of transition experiments in the ONERA R2Ch hypersonic wind tunnel. Flow conditions are summarised in table 1. The free stream Mach number  $M_{\infty}$  is equal to 6 and the unit Reynolds number  $Re_1$  is equal to  $10.8 \times 10^6 \, \mathrm{m}^{-1}$ . The plate has a length of  $L_X = 0.75 \, \mathrm{m}$  and is modelled as an isothermal wall at  $T_W = 300 \, \mathrm{K}$  leading to a wall to recovery temperature ratio  $T_W/T_\Gamma$  of 0.60.

**Table 1.** Flow conditions.

$M_{\infty}$	$P_{i\infty}$	$T_{i\infty}$	$Re_1$	$T_w/T_r$
6	15 × 10 <sup>5</sup> Pa	550 K	$10.8 \times 10^6  \mathrm{m}^{-1}$	0.60

# 2.2. Resolvent-based linear stability analysis

In order to excite specific instabilities in the boundary layer to trigger the transition to turbulence, a stability analysis of the laminar flow is performed. The objective is to identify the most amplified perturbations and to compute their associated optimal forcing vectors. A global linear stability analysis is performed using BROADCAST, an ONERA open-source linear stability toolbox [14]. The compressible Navier-Stokes equations are linearised for small perturbations  $\mathbf{q}'$  around a laminar base-flow, and forcing terms  $\mathbf{f}'$  are introduced:

$$\partial_t \mathbf{q}' = \mathcal{J} \mathbf{q}' + \mathbf{f}' \tag{1}$$

where  $\mathcal J$  is the Jacobian operator. Assuming that the linear forcing and response vectors are harmonic in space (span direction) and time,  $\mathbf f'$  and  $\mathbf q'$  can be written as:  $\mathbf f' = e^{i(\omega t + \beta z)}\hat{\mathbf f}$  and  $\mathbf q' = e^{i(\omega t + \beta z)}\hat{\mathbf q}$  with angular frequency  $\omega$  and transverse wavenumber  $\beta$ , and the resolvent operator  $\mathcal R = (i\omega \mathbf I - \mathcal J)^{-1}$ 

can be introduced:

$$\hat{\mathbf{q}} = \mathcal{R}\hat{\mathbf{f}} \tag{2}$$

The optimal perturbation and its associated response are obtained when the gain  $\mu$  between the forcing energy  $\|\hat{\mathbf{f}}\|_F$  and the response energy  $\|\hat{\mathbf{q}}\|_E$  is maximised. One can thus build the following optimisation problem:

$$\mu^{2} = \sup_{\hat{\mathbf{f}}} \frac{\|\hat{\mathbf{q}}\|_{E}^{2}}{\|\hat{\mathbf{f}}\|_{E}^{2}} = \sup_{\hat{\mathbf{f}}} \frac{\|\mathcal{R}\hat{\mathbf{f}}\|_{E}^{2}}{\|\hat{\mathbf{f}}\|_{E}^{2}}$$
(3)

Chu's disturbance energy and its associated norm  $\|\cdot\|_{Chu}$  are used for this study. Solving the optimisation problem provides the optimal forcing vector and the associated energy gain for a given frequency and a given transverse wavenumber. Computing the optimal gain for a range of frequencies and wavenumbers enables to draw a gain map that highlights the most linearly amplified modes.

Computation of the two-dimensional base-flow is performed using an iterative pseudo-Newton method. BROADCAST uses a seventh-order-accurate scheme for inviscid fluxes and a fourth-order compact scheme for viscous fluxes, computation of the Jacobian matrix is performed with algorithmic differentiation. The computational domain is restricted to a length of  $0.27L_{\rm X}$  from the leading edge of the flat plate, as non-linear mechanisms are expected to take place further downstream during the DNS of transitional flows. The inflow boundary condition is prescribed using a preliminary two-dimensional compressible boundary layer simulation, which follows the same numerical setup as the one detailed for the three-dimensional simulations in section 2.3., and is also used to initialise the computation of the base-flow.

#### 2.3. Direct numerical simulations

To simulate the transitional and turbulent boundary layer flow, the compressible Navier-Stokes equations are solved using Fast (Flexible Aerodynamic Solver Technology), an in-house ONERA HPC solver [15]. Viscous fluxes are discretised with a second-order-accurate central scheme, while convective fluxes are solved using an AUSM-type scheme associated to a fifth-order MUSCL reconstruction and a shock sensor. Time integration is conducted with a three-steps low-storage Runge-Kutta method. The simulation time step is set to  $6 \times 10^{-9} \, \mathrm{s}$  to maintain a CFL number of less than 0.5 in the whole domain.

The length  $L_{x}$  of the domain has been chosen to simulate a sufficiently large turbulent region downstream of the transitional region, so that noise radiated by a fully turbulent region can be studied. In order to accommodate periodic boundary conditions on the side walls, the domain width  $L_z$  is equal to seven times the transverse wavelength of the most amplified oblique perturbation mode highlighted in the stability analysis (see section 3.1.). This represents about four times the maximum turbulent boundary layer thickness. A two-point velocity correlation has been computed for several spanwise stations to ensure that the width of the domain is large enough for turbulent structures to be spatially decorrelated. The numerical domain is discretised in accordance with DNS resolution criteria [16]:  $\Delta x^+ < 8$ ,  $\Delta y_{wall}^+ < 8$ 0.5,  $\Delta z^+ < 5$ . Points are uniformly distributed in the spanwise direction. Near the leading edge, the streamwise cell size is refined following a geometric distribution. In the wall-normal direction, points are distributed following a geometric distribution in the boundary layer zone, a uniform distribution is used in the region of acoustic perturbation propagation with a cell height of 2% of the maximum boundary layer thickness. Above this region, the cell size then expands until the upper limit of the domain. This leads to a grid size close to one billion points. A short region with a symmetry boundary condition at the wall is added upstream of the leading edge to avoid interferences between the uniform inflow and the no-slip condition on the plate. The characteristics of the computational domain are summarised in table 2, and a visualisation of the mesh is shown in figure 1.

**Table 2.** Computational domain characteristics. Lengths in meters, duration in seconds.

L <sub>x</sub>	Ly	Lz	N <sub>X</sub>	$N_y$	Nz	Δt
0.75	0.15	0.044	4515	568	360	$6 \times 10^{-9}$

Perturbations are included in the simulation through the use of volume time-depending source terms for density, momentum and stagnation energy density. Three cases are presented in this paper, implementing three forcing scenarios: two cases using resolvent modes highlighted during the stability analysis, and a random-based approach.

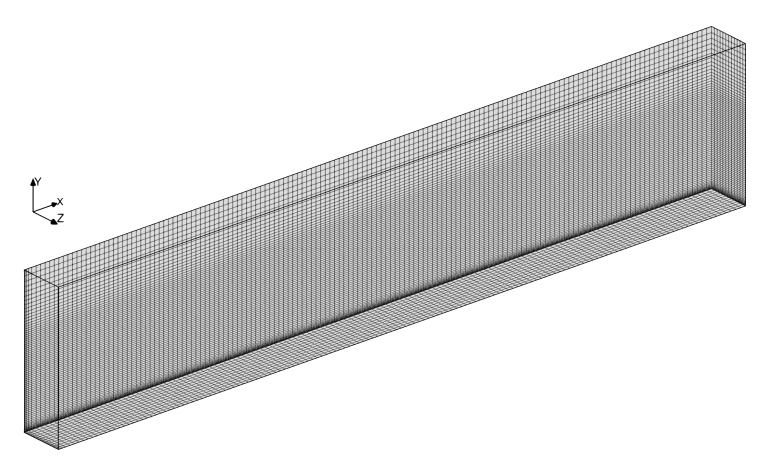


**Fig 1.** Visualisation of the computational mesh. For visualisation purpose, one point over thirty is plotted in the x and z-directions and one point point every seven is plotted in the y-direction.

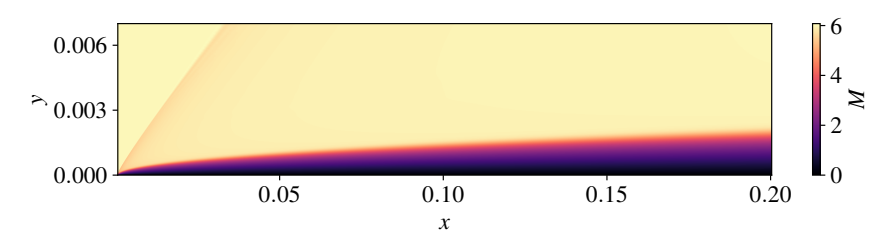


Fig 2. Base-flow Mach number contour, the visualisation is restricted to the near wall region.

A resolvent mode  $\hat{\mathbf{f}}$  can be used to compute volume, time depending forcing terms:

$$\mathbf{f}'(x, y, z) = Ae^{i\omega t + \beta z} \hat{\mathbf{f}}(x, y) + c.c. \tag{4}$$

where c.c. denote the complex conjugate and A is an arbitrary amplitude factor.

In the random forcing case, the forcing region starts  $0.013L_{\rm X}$  downstream of the leading edge, has a streamwise length of  $0.013L_{\rm X}$  and extends vertically until the local boundary layer edge. Each source term variable is sampled from a normal Gaussian distribution, and is then Gaussian filtered over a seven-cell kernel to attenuate strong cell-to-cell gradients. Forcing terms are updated every 15 iterations resulting in an update frequency of 11 MHz which is two orders of magnitude higher than the highest frequencies of the amplified modes highlighted by the resolvent stability analysis (see section 3.1.). The amplitude of the noise  $A_n$  has been adjusted so that the transition location is similar to what has been achieved in the two previous cases. Comparing with the density forcing  $\mathbf{f}'$  used in the first Mack mode forcing case:  $A_n/\max|\mathbf{f}'| \approx 3$ .

# 3. Results

#### 3.1. Amplified perturbations in a laminar flat plate hypersonic boundary layer

The laminar base-flow computation requires less than ten iterations of the pseudo-Newton method to decrease the  $L^2$  residuals by 12 orders of magnitude, starting from a solution initialised with Fast as detailed in section 2.2.. A Mach number contour of the base-flow is shown in figure 2.

The resolvent stability analysis is performed for a wide range of frequencies and transverse wavenumbers, leading to the gain map shown in figure 3, in which two dominantly amplified modes can be identified. The most amplified one shows a gain peak at  $(f, \beta) = (194 \, \text{kHz}, 0 \, \text{m}^{-1})$ . This two-dimensional mode corresponds to the second Mack mode, and its associated forcing and response vectors are illustrated in figure 4a with density forcing and response fields. The gain map also shows a second dominant perturbation which is an oblique mode with a maximal gain found for  $(f, \beta) = (38 \, \text{kHz}, 992 \, \text{m}^{-1})$ . This mode corresponds to the first Mack mode, its density forcing and response vectors are illustrated in figure 4b.

Fig 3. Frequency-transverse wavenumber gain map.

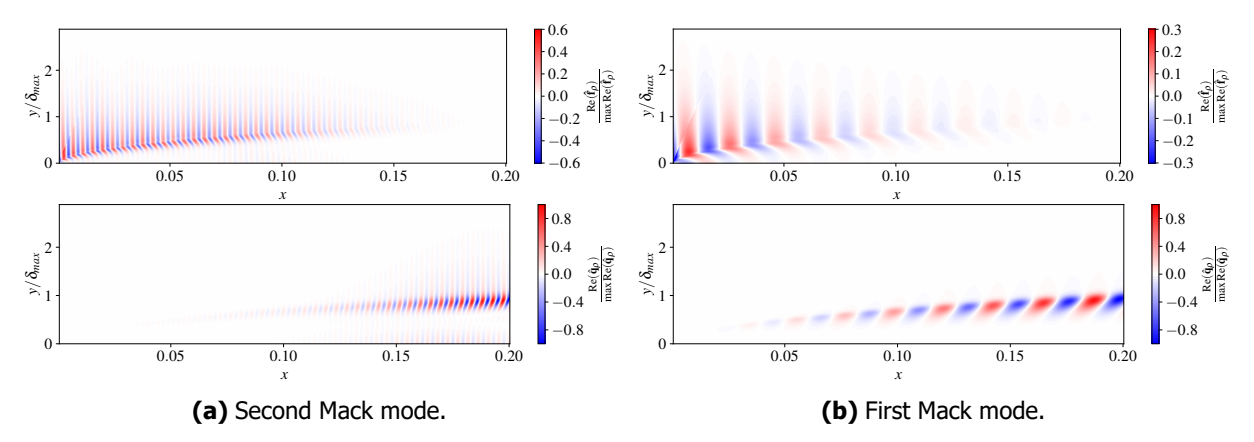


Fig 4. Max-normalised real part of density forcing (top) and response (bottom) vectors.

These two perturbation modes will be used in the next section to compute time-dependent volume forcing terms to trigger the transition to turbulence in DNS.

For the first resolvent-based case, the first Mack mode is used. Even if the resolvent analysis has shown that this mode is less amplified than the second Mack mode, its strong oblique nature is preferred over the two-dimensional character of the second Mack mode in order to promote the growth of three-dimensional structures in the transition region. Time dependent volume forcing terms are constructed from the first Mack mode optimal forcing vector as the superposition of positive and negative transverse wavenumber contributions:

$$\mathbf{f}'(x, y, z) = 2A\cos(\beta z)e^{i\omega t}\hat{\mathbf{f}}(x, y) + c.c.$$
 (5)

The amplitude factor A has been adjusted to set the transition onset location at around  $0.27L_X$ , ensuring that a sufficiently large noise radiating region develops in the extent of the domain. A visualisation of the source terms is shown in figure 5.

A second resolvent-based case has been set up using both the first and second Mack modes to compute the source terms. As shown in the figure 3, the maximum gain for the second Mack mode is achieved for a purely two-dimensional forcing. However, three-dimensionality is preferred to promote transition to turbulence. Thus, in this section the second Mack mode is forced using a non-zero transverse wavenumber  $\beta_2$  chosen so as to be compatible with the periodic boundary conditions imposed on the sides of the domain:  $\beta_2 = 2\pi/L_z = 142 \, \text{m}^{-1}$ . The corresponding oblique resolvent mode still provides a high energy gain, as shown in resolvent gain map. Similarly to what has been used for the first Mack mode case, the second Mack mode contribution of the source terms is computed as a superposition of positive and negative wavenumber forcing fields. A visualisation of the oblique second Mack mode resolvent forcing and response vectors is shown in figure 6, alongside a visualisation of the forcing and linear response corresponding to the superposition of positive and negative transverse wavenumbers contributions. Preliminary simulations have shown that even though three-dimensionality is introduced with this method, a first mode contribution is still needed to trigger the transition of the boundary layer within the extent of the domain. Summing contributions from the first and second Mack modes, the source

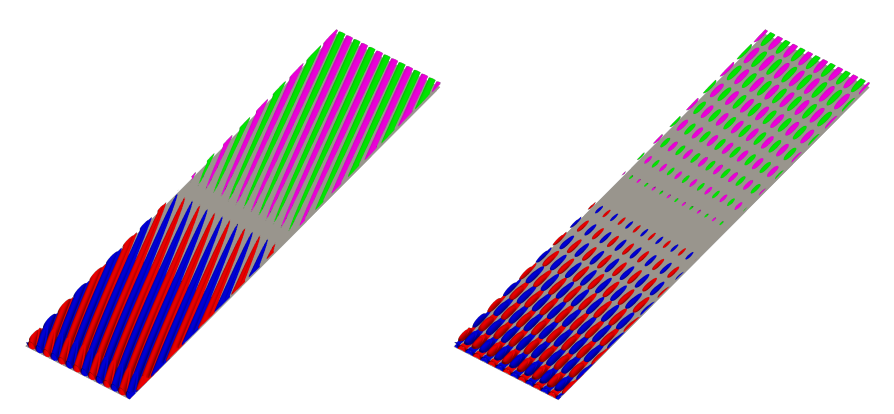


**Fig 5.** Qualitative visualisation of first Mack mode density forcing (red/blue) and density linear response (magenta/green) for a length of  $0.27L_{\times}$ . Left: positive transverse wavenumber. Right: superposition of positive and negative transverse wavenumbers, as used for the DNS source terms.

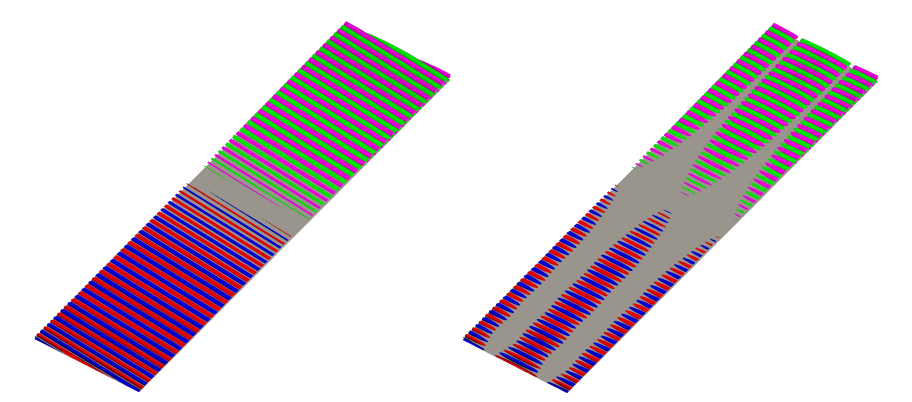


**Fig 6.** Qualitative visualisation of second Mack mode density forcing (red/blue) and density linear response (magenta/green) for a length of  $0.27L_{\rm X}$ . Left: positive transverse wavenumber. Right: superposition of positive and negative transverse wavenumbers, as used for the second Mode contribution to DNS source terms.

terms are computed as:

$$\mathbf{f}'(x, y, z) = 2A_1 \cos(\beta_1 z) e^{i\omega_1 t} \hat{\mathbf{f}}_1(x, y)$$

$$+ 2A_2 \cos(\beta_2 z) e^{i\omega_2 t} \hat{\mathbf{f}}_2(x, y) + c.c.$$
(6)

where  $\cdot_1$  and  $\cdot_2$  refer to first Mack mode and second Mack mode quantities respectively. Compared to the previous section, the amplitude of the first Mack mode has been reduced by 30%, and the amplitude ratio between first and second Mack modes is  $A_1/A_2 = 0.175$ .

# 3.2. Transitional and turbulent boundary layer simulations

## 3.2.1 Overall description of the flow fields

The amplitudes of the forcing terms have been adjusted to provide similar transition onset locations for all three cases, in order to compare flow properties of interest. One way to compare the transition location is to plot the time and span-averaged skin friction coefficient along the plate. Figure 7 displays these values, along with laminar and turbulent skin friction laws computed for a compressible flat plate boundary layer [17]. The random-based approach yields a smooth transition between the laminar and turbulent regime, while the resolvent mode-based approaches are characterized by steeper departures from the laminar region, a higher overshoot, and irregularities in the  $C_f$  evolution that could indicate the presence of stationary phenomena, especially for the first Mack mode case.

For all three cases, qualitative visualisations of the instantaneous flow solutions are presented in figure 8. *Q*-criterion iso-surfaces are drawn and coloured by the local flow velocity, and density gradient

**Fig 7.** Span and time-averaged skin friction coefficient along the plate.

magnitude slices are added on the  $x=x_{max}$  and z=0 planes. They highlight the formation of turbulent structures downstream of the transition onset location until a fully turbulent boundary layer is obtained. Instantaneous density gradient magnitude slices are presented separately in figure 9, where acoustic radiation from the transitional and turbulent regions is visible. For the resolvent forcing cases, regular patterns are observed in the acoustic radiation originating from the transition region, reflecting the time-periodic nature of the forcing terms. For the third case, the noise radiated by the transition region doesn't show any spatial periodicity, reflecting the random nature of the forcing. For all three cases, the disturbances radiated by the turbulent region exhibit the expected strong directionality, with a wavefront angle of about 60° from the horizontal direction.

#### 3.2.2 Pressure fluctuations

Wall-normal profiles of root mean square value of pressure fluctuations are extracted at the end of the computational domain and shown in figure 10. For all three cases, the fluctuation levels remain fairly uniform at 2.5 - 3 % outside of the boundary layer up until four boundary layer thicknesses away from the wall, where the noise radiation starts to originate from the transition region. The uniformity of the pressure fluctuation levels is coherent with available experimental and numerical data [7, 9]. In the first mode forcing case, fluctuation levels originating from the transition region show a non-homogeneous pattern with a general decreasing trend until the levels drops to near zero value outside of the region affected by noise radiated by the transition and turbulent regions. In the second resolvent-based case, levels are similar but show a smoother profile in the region where noise is radiated from the transition region, even though some non-regular patterns can be found. Those could be related to the stationary structures mentioned in section 3.2.1 regarding the skin friction coefficient evolution along the plate. For the random forcing case, pressure fluctuation levels are found to be higher than those computed with the Mack mode forcing cases. A peak is found at  $y/\delta \approx 8$ , which is where noise radiation originates from the region round x = 25 cm, indicating strong noise radiation from the transition region. For this case, non-zero fluctuation levels are found higher in the profile, indicating that noise-emitting structures arise earlier. This could be related to the earlier departure from the laminar state shown in figure 7 and 8. For the resolvent-based cases, a spot of non-zero fluctuation is found at  $v/\delta \approx 10.5$ . It could be caused by local interactions between the laminar boundary layer and the forcing terms, near the leading edge. This spot is weaker for the first and second Mack mode case. Because of the second Mack mode contribution to the source terms, the amplitude of the first Mack mode (reflected by  $A_1$  in equation 6) was reduced in this simulation, which could explain this attenuation.

The spectral content of pressure fluctuations has been studied at the wall and in the free stream region at six longitudinal locations distributed on the x-axis, starting  $0.067L_x$  downstream of the leading edge and spaced in the x-direction by a length of  $0.2L_x$ . Free stream data are extracted at a height of about  $2\delta_{max}$ . Power spectral densities of wall and free stream pressure fluctuations are presented in figure 11 for the first Mack mode case, figure 12 for the first and second mode forcing case and figure 13 for the random forcing case.

Wall pressure fluctuation spectra for the resolvent-based cases exhibits peaks in the transition region corresponding to the resolvent modes (38 kHz and 194 kHz for the first and second Mack modes, respectively) and higher harmonics. In the spectrum corresponding to the random forcing case, a peak observed at  $x=5\,\mathrm{cm}$  suggests that the random forcing has excited an unstable mode. As the PSD extraction location moves downstream, the spectrum gains broadband content. At  $x=20\,\mathrm{cm}$ , one peak

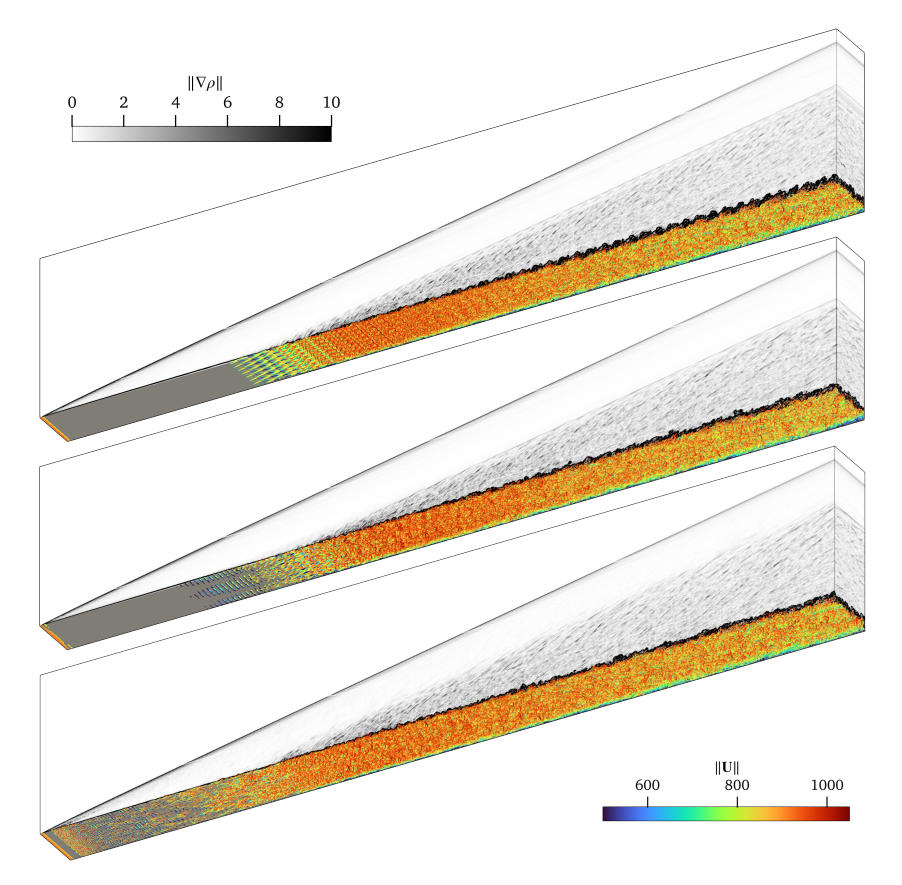


**Fig 8.** Density gradient magnitude slices (z = 0 and  $x = x_{max}$ ) and Q-criterion isosurfaces coloured by local velocity magnitude. From top to bottom: first Mack mode forcing case, first and second Mack mode forcing case, random forcing case.

can still be distinguished at  $f \approx 200 \, \text{kHz}$ , which corresponds to the frequency of the second Mack mode that has been highlighted during the resolvent linear stability analysis performed on the first 20 cm of the plate, and is the most linearly unstable mode. Furthermore, in a close-up view of Q-criterion visualisation focused on the first 15 cm of the domain shown in figure 14, quasi-two-dimensional structures seem to appear, with a wavelength similar to that of the second Mack mode forcing vector computed during the linear stability analysis. This suggests that the random forcing could have excited a second Mack mode instability. For all three cases, as the flow reaches a turbulent state, the wall-extracted spectra gain broadband content until the boundary layer is fully turbulent.

Regarding the free stream spectra of the resolvent forcing cases, peaks corresponding to the Mack modes and their harmonics are observed in the regions where the noise radiation originates from the transition region. Further downstream, where the perturbations are radiated by regions of more turbulent flow, the spectral content gains broadband content. At the most aft location, the spectrum exhibits a quasi-fully broadband nature. For the random-based case, the spectrum extracted at  $x=20\,\mathrm{cm}$  shows a uniform level until around 220 kHz, before dropping for higher frequencies. The Mach line crossing this extraction point originates from the wall at  $x=11.8\,\mathrm{cm}$ , where the boundary layer is still fairly laminar (see figure 7) and where little acoustic radiation from the boundary layer is expected. The uniform nature of the spectrum could thus be due to the noise radiation from the random forcing region near the leading edge. For the more downstream stations, the extracted spectra show a broadband behaviour, as observed for the two other cases.

The convection velocity of the perturbations  $U_c$  has been computed for the first Mack mode case along a wall-normal profile at the end of the computational domain, and is shown in figure 15. This velocity is computed from the time delay that maximises the space-time correlation between two probes separated in the computational domain by a spacing  $\Delta x$ . Outside of the boundary layer,  $U_c$  is found to be around 0.65 times the free stream velocity, which is coherent with experimental data from Laufer [7] and previous DNS works [9]. According to the eddy Mach wave radiation model, assuming that this convection velocity corresponds to the velocity of the acoustic sources implies that the Mach waves must be oriented

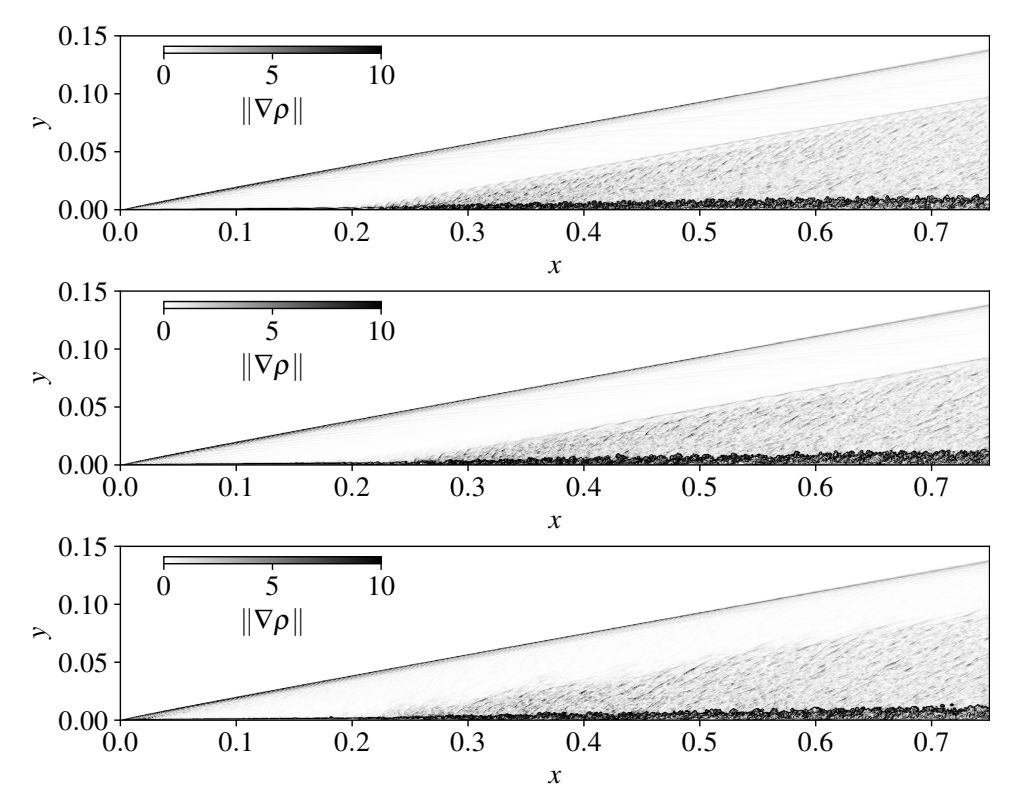


**Fig 9.** z-normal slice coloured by density gradient magnitude. From top to bottom: first Mack mode forcing case, first and second Mack mode forcing case, random forcing case.

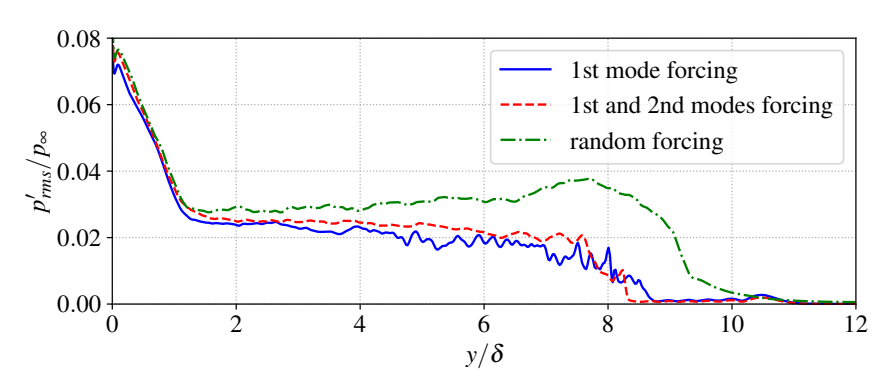


Fig 10. Wall-normal pressure fluctuation level profile extracted at the end of the domain.

around 60° from the horizontal axis, which agrees well with the density gradient magnitude slices in figure 9.

#### 3.2.3 Entropy variation

The time-averaged variation of entropy has been computed and extracted along a horizontal line 3 cm  $\approx 2.7 \delta_{max}$  above the wall. Figure 16 shows the comparison of entropy variation for the three cases and for a laminar simulation performed without forcing terms. The figure is complemented with the entropy jump computed for a  $10.52^{\circ}$  oblique shock wave, corresponding to the angle of the leading edge shock wave measured from the density gradient magnitude slices in figure 9. The laminar solution shows little entropy increase downstream of the leading edge shock, while the three turbulent cases exhibit stronger entropy increases, with similar trends. For all three cases, a stronger entropy increase is found in the area where noise radiation originates from the transition region, indicating that stronger perturbations are generated in this region of the boundary layer. Further downstream, the entropy still increases but with a lower rate. The similarity between the three curves indicates that the choice of the forcing scenario has little importance regarding this aspect of the pressure fluctuations.

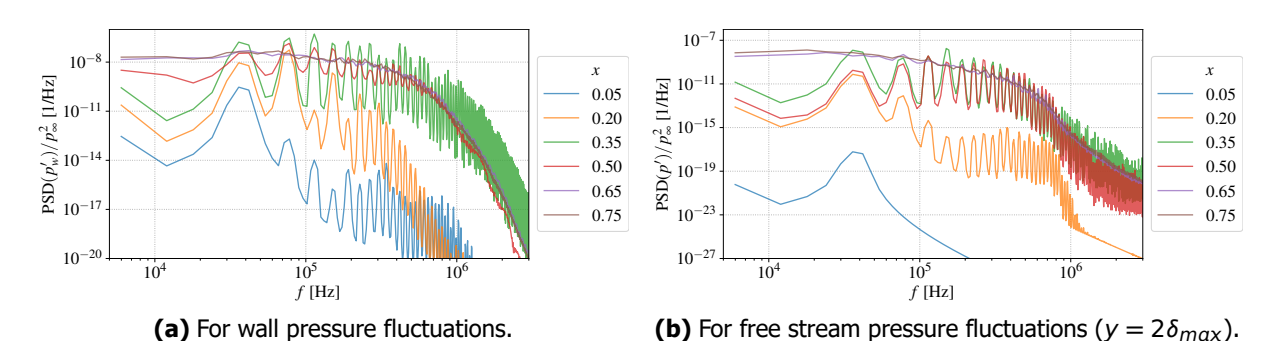
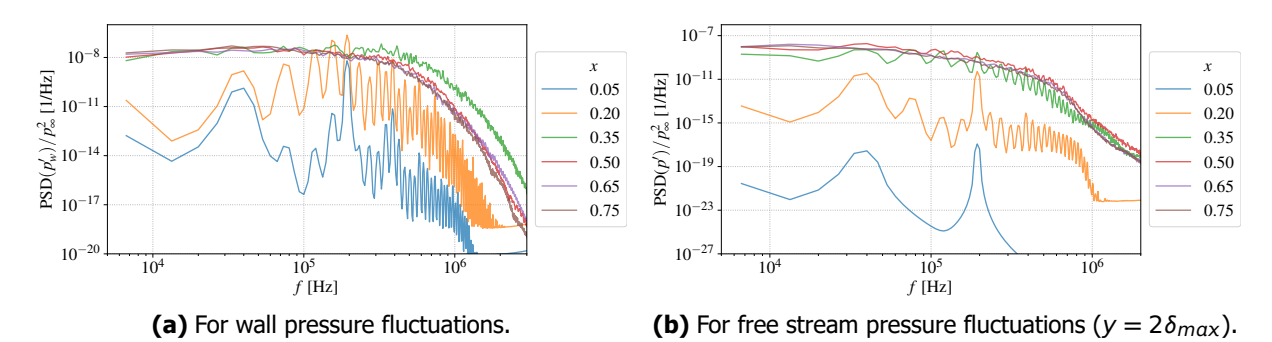


Fig 11. Power spectral density of pressure fluctuations from the first Mack mode forcing case.



**Fig 12.** Power spectral density of pressure fluctuations extracted from the first and second Mack modes forcing case.

#### 4. Conclusion

DNS has been used to simulate the transition to turbulence of hypersonic boundary layers over a flat plate in flow conditions representative of hypersonic wind tunnel test conditions. This geometry has been chosen to provide a canonical case to set up tools and methods for the numerical investigation of acoustic perturbations radiated by nozzle wall turbulent boundary layers in hypersonic wind tunnels. A resolvent-based linear stability analysis has highlighted that the first and second Mack modes are the dominant perturbation modes in the laminar base-flow. Then, three DNSs of transition have been performed. In the first two cases, optimal forcing vectors associated to the first and second Mack modes are used to compute volume time-depending source terms, which trigger the transition of the boundary layer. The third case implements a random forcing approach in a restricted region near the leading edge. For all cases, adjusting the amplitude of the forcing terms enables to obtain similar transition locations. Simulations have allowed to study the acoustic radiation from the transitional and turbulent regions. The pressure fluctuations radiated by the fully turbulent regions show uniform RMS levels, and density magnitude slices highlight the strong directionality of the wavefronts, which is coherent with the eddy Mach wave radiation model and with perturbation convection velocity calculations. Spectral analysis of wall and free stream pressure fluctuations shows that both wall and free stream spectra gain broadband content as the location moves downstream. When using a harmonic forcing, the frequency peaks observed in the transition region at the wall are reflected in the noise radiation frequency content. Overall, similar characteristics are found for acoustic perturbations radiated by the turbulent region of the flow regardless of the forcing scenario. Future work will focus on further analysing currently acquired numerical data, and on setting up a workflow for extraction/injection of acoustic perturbations to simulate the effect of wind tunnel-like free stream disturbances on a laminar boundary layer.



This work was financially supported by the French Ministry of Armed Forces – Defence Innovation Agency (AID), as part of a PhD program. Simulations were performed on the TGCC Irene supercomputer under the GENCI allocation A0172A15716.

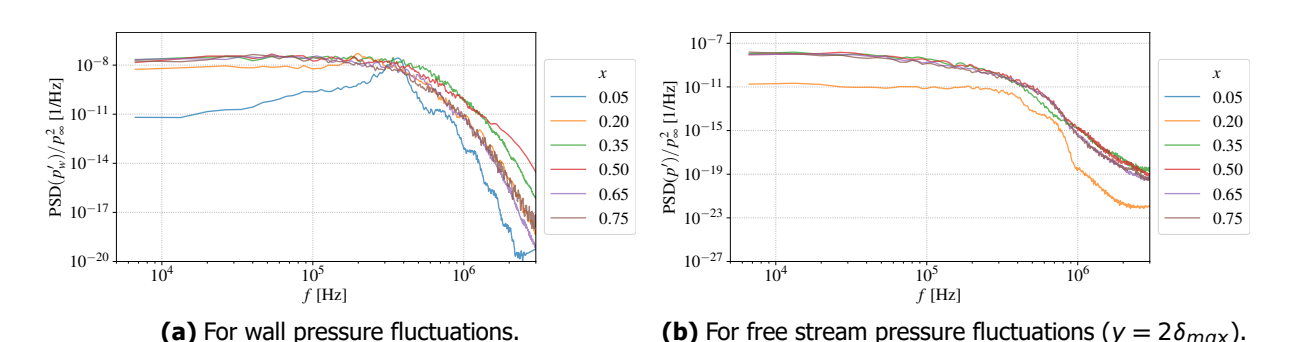
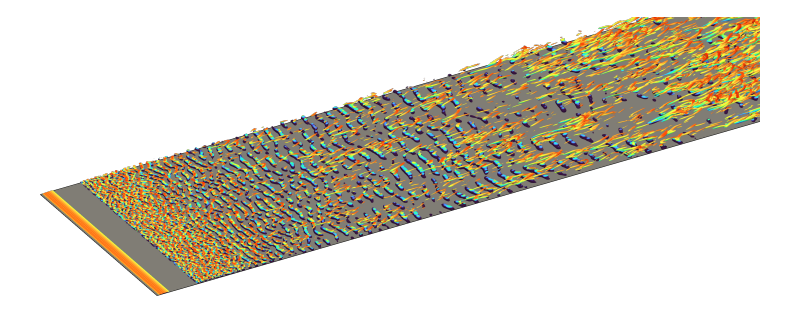


Fig 13. Power spectral density of pressure fluctuations extracted from the random forcing case.



**Fig 14.** Density gradient magnitude slices and Q-criterion isosurface coloured by local velocity magnitude for the random forcing case, close-up view starting at the leading edge of the plate and extending for a length of  $0.2L_X$ .

#### References

- 1. Berry, S. et al. Boundary Layer Control for Hypersonic Airbreathing Vehicles in 34th AIAA Fluid Dynamics Conference and Exhibit (2004).
- 2. Van Driest, E. R. The Problem of Aerodynamic Heating. Aeronaut. Eng. Rev. 48 (1956).
- 3. Schneider, S. P. Effects of High-Speed Tunnel Noise on Laminar-Turbulent Transition. J. Spacecr. Rockets 38 (2001).
- 4. Kovasznay, L. S. G. Turbulence in Supersonic Flow. en. J. Aeronaut. Sci. 20 (1953).
- 5. Morkovin, M. V. On Transition Experiments at Moderate Supersonic Speeds. J. Aeronaut. Sci. 24 (1957).
- 6. Laufer, J. Aerodynamic Noise in Supersonic Wind Tunnels. en. J. Aerosp. Sci. 28 (1961).
- 7. Laufer, J. Sound radiation from a turbulent boundary layer in Colloque International sur la Mécanique de la Turbulence (1962).
- 8. Phillips, O. M. On the generation of sound by supersonic turbulent shear layers. J. Fluid Mech. 9 (1960).
- 9. Duan, L. et al. Pressure fluctuations induced by a hypersonic turbulent boundary layer. J. Fluid Mech. 804 (Oct. 10, 2016).
- 10. Hildebrand, N. et al. Reynolds-Number Effects on the Acoustic Disturbance Environment in a Mach 6 Nozzle. AIAA J. 61 (2023).
- 11. Huang, J. et al. Direct Numerical Simulation of Acoustic Noise Generation from the Nozzle Wall of a Hypersonic Wind Tunnel in 47th AIAA Fluid Dynamics Conference (June 5, 2017).
- 12. Morkovin, M. V. Transition in open flow systems-a reassessment. Bull. Am. Phys. Soc. 39 (1994).
- 13. Lugrin, M. On the use of random inflow disturbances to simulate transitional hypersonic wind tunnel experiments in HISST: 2nd International Conference on High-Speed Vehicle Science & Technology (2022).
- 14. Poulain, A. et al. BROADCAST: A high-order compressible CFD toolbox for stability and sensitivity using Algorithmic Differentiation. Comput. Phys. Commun. 283 (2023).

**Fig 15.** Relative convection velocity wall-normal profile near the outlet of the domain. The dataset has been averaged on the spanwise direction.

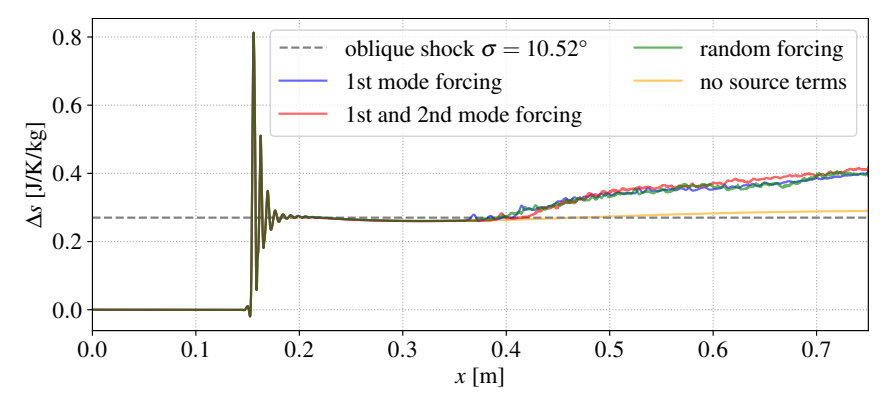


Fig 16. Time-averaged entropy variation.

- 15. Peron, S. et al. An immersed boundary method for preliminary design aerodynamic studies of complex configurations. 23rd AIAA Computational Fluid Dynamics Conference (2017).
- 16. Poggie, J. et al. Resolution effects in compressible, turbulent boundary layer simulations. Comput. Fluids 120 (2015).
- 17. Cousteix, J. Aérodynamique : Turbulence et couche limite (Cépaduès Éditions, Toulouse, 1989).